



# Modeling dynamics of chemical reaction networks using electrical analogs: Application to autocatalytic reactions

Sarang S. Nath<sup>a,\*</sup>, John Villadsen<sup>b</sup>

<sup>a</sup> The Novo Nordisk Foundation Center for Biosustainability, Technical University of Denmark, Lyngby 2800, Denmark

<sup>b</sup> Department of Chemical and Biochemical Engineering, Technical University of Denmark, Lyngby 2800, Denmark

## ARTICLE INFO

### Keywords:

Autocatalysis  
Network theory  
Modeling and computer simulation  
Electrical circuits  
Chemical kinetics  
Nonlinear dynamics  
Molecular mechanism  
Biological implications

## ABSTRACT

Modeling complex chemical reaction networks has inspired a considerable body of research and a variety of approaches to modeling nonlinear pathways are being developed. Here, a general methodology is formulated to convert an arbitrary reaction network into its equivalent electrical analog. The topological equivalence of the electrical analog is mathematically established for unimolecular reactions using Kirchhoff's laws. The modular approach is generalized to bimolecular and nonlinear autocatalytic reactions. It is then applied to simulate the dynamics of nonlinear autocatalytic networks without making simplifying assumptions, such as use of the quasi-steady state/Bodenstein approximation or the absence of nonlinear steps in the intermediates. This is among the few papers that quantify the dynamics of a *nonlinear* chemical reaction network by generating and simulating an electrical network analog. As a realistic biological application, the early phase of the spread of COVID-19 is modeled as an autocatalytic process and the predicted dynamics are in good agreement with experimental data. The rate-limiting step of viral transmission is identified, leading to novel mechanistic insights.

## 1. Introduction

Chemical and biochemical reaction networks [1,2] have been studied extensively in chemical engineering, given their great fundamental and industrial importance. Studies have been carried out on high-temperature chemical reactions [3,4], chemical reactions in crowded cellular environments [5], metabolic and regulatory networks [2,6], reactions in various reactor configurations [7], and reaction pathways in disease [8]. Various experimental and mathematical modeling techniques and approaches have been used to elucidate network dynamics based on chemical and biochemical reaction chemistry and engineering [1–4,7], machine learning [6], isotopic labeling [8], the theory of dynamical systems [9], control theory [10,11], and network and graph theory [2,12].

Only a small subset of the above studies have focused on nonlinear and coupled chemical and biological systems that reveal interesting spatial and temporal dynamics, oscillations, and limit cycles. These have been analyzed by diverse approaches from metabolic engineering [2, 5–8], nonlinear dynamics and chaos theory [9], electrical circuit and control theory [10,11], fuzzy logic and graph theory [2,12], polymer science [13], and nanotechnology [14].

Autocatalytic reactions constitute an important area of contemporary chemical and biological reaction chemistry and engineering research. Since the pioneering work of Gray and Scott on nonlinear autocatalysis as a model system that exhibits dynamic complexity [15], several systems of single autocatalytic chemical reactions with different kinetics have been studied extensively in the field [16,17]. The common theme linking these papers is the analysis of a single autocatalytic reaction in an isothermal continuous stirred tank reactor [15–17]. Only recently have coupled reactions and networks been treated [18,19], but a general methodology that quantitatively models the dynamics of such nonlinear networks is still under development [19].

In our research program, we have been seeking to formulate a general and modular methodology that can represent, visualize, and quantify the dynamics of nonlinear chemical reaction networks. Conversion to topologically-equivalent electrical circuit analogs appeared to provide a promising approach that satisfied the above criteria. However, there were formidable difficulties in constructing such analogs.

The difficulties in converting chemical reaction networks to equivalent electrical circuits mentioned above mainly arose from the fundamental differences in *structure* between potential and kinetic theory. The difference in potential between any two points A and B on a potential

\* Corresponding author.

E-mail addresses: [sasuna@biosustain.dtu.dk](mailto:sasuna@biosustain.dtu.dk), [nathsarang@gmail.com](mailto:nathsarang@gmail.com) (S.S. Nath).

<https://doi.org/10.1016/j.cej.2022.100374>

Available online 29 July 2022

2666-8211/© 2022 The Authors. Published by Elsevier B.V. This is an open access article under the CC BY-NC-ND license (<http://creativecommons.org/licenses/by-nc-nd/4.0/>).

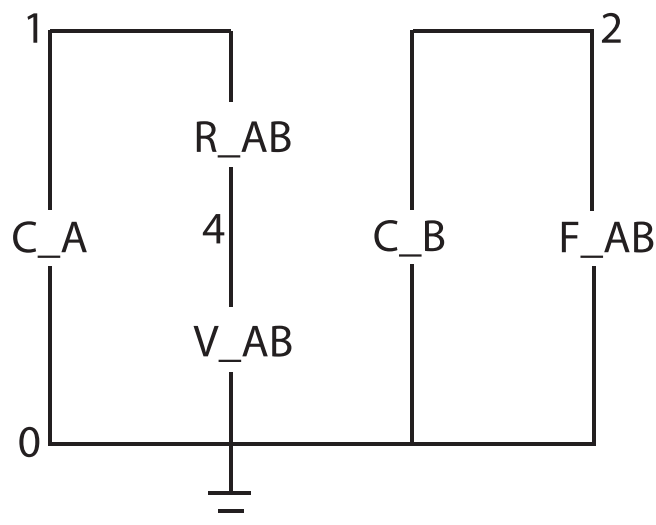


Fig. 1. Electrical analog of the irreversible reaction  $A \xrightarrow{k} B$ . R and C represent a resistor and capacitor respectively, V represents a voltage source, and F represents a current-controlled current source.

energy surface is a measure of the force; reversing the external constraints such that A becomes B and vice versa leads to a measured force (and flow of current) of the same magnitude but of opposite sign compared to the first experiment. Now consider a reversible chemical reaction  $A \rightleftharpoons B$  in the framework of a kinetic theory. A certain reaction rate is measured with concentrations  $C_A$  of reactant and  $C_B$  of product. Reversing the concentrations, however, does not yield a rate that is simply equal to and negative of the rate measured previously.

Luyben [11] surveyed developments in control systems engineering over the decades as follows: “In the 1960s, chemical engineers began to apply dynamic analysis and control theory to chemical engineering processes. Most of the techniques were adapted from the work in the aerospace and electrical engineering fields, including the concept of examining the many parts of a complex plant together as a single unit, with all the interactions included, and devising ways to control the entire plant by a control systems engineering. The current popular “buzz” words *artificial intelligence* and *expert systems* are being applied to these types of studies” [11]. Wiechert reviewed various kinetic models for metabolic engineering and found that the predictive power of “some types of metabolic models is currently not very high” [20]. He suggested that electrical circuits be used in the modeling “because they have much in common with chemical reaction networks” [20]. Ederer and Gilles [21] attempted to develop thermodynamically-consistent kinetic models of reaction networks. They noted that “an analogy to electrical networks becomes obvious in their relations between thermokinetic potentials and concentrations” [21]. However, none of the above-cited [11,20,21] or other works showed how to create topologically-equivalent circuit analogs for the chemical reaction networks by use of standard electrical elements. Furthermore, none of the works has actually *simulated* electrical circuits to obtain the network dynamics. In particular, we could not find papers that quantitatively model the dynamics of *nonlinear* reaction networks using electrical circuits.

In this work, we have developed a novel methodology that surmounts the above barriers and converts a chemical reaction network into a topologically-equivalent electrical circuit using various electrical elements. The elements are added to the electrical analog in a modular way. First, the equivalent electrical network is tested on simple unimolecular and series reactions. Then, Kirchhoff’s laws establish the topological equivalence of the generated electrical analog with the simple chemical reaction network (Section 2). It is further verified that the simulated electrical analog leads to the correct dynamics as obtained by

the exact mathematical solution of the simple chemical reaction systems (Section 2).

Upon verification of the dynamics for simple systems, the procedure is extended to single autocatalytic systems of irreversible and reversible reactions (Section 3). Thereafter we turn to nonlinear reaction networks consisting of autocatalytic reactions. The nonlinear circuit analog of the Brusselator scheme of autocatalytic reactions [22,23] is developed and explained in considerable detail (Section 4). The phase diagram for the nonlinear autocatalytic network of the Brusselator is generated with the help of a stability analysis (Section 5). Then the electrical circuit analog is simulated (Section 6). The usual simplifying assumptions that are employed in other analyses, such as use of the quasi-steady state/-Bodenstein approximation or the absence of nonlinear steps in the intermediates [23,24] (for a detailed discussion of these assumptions see Ref. [25]), are not made by our method, and the nonlinear dynamics of the system such as chemical oscillations and limit cycles are characterized by the new network approach by use of electrical simulation software [26]. This is the first paper in the literature that quantifies the dynamics of a *nonlinear* chemical reaction network by generation and simulation of an electrical network analog.

It is then shown that the developed methods can be applied to other autocatalytic processes. As an example of a particularly relevant problem, the spread of COVID-19 is treated by chemical reaction engineering principles in Section 7. The viral transmission process has been modeled classically by first-order rate laws leading to exponential spread, as in the well-known Susceptible-Infectious-Removed (SIR) reaction scheme [27]. Recent embellishments have used an exponential spread with additional parameters [28], coupled first-order reactions [29], combinations of exponential and power laws [30], or analogy with residence time distributions [31]. We have modeled the early phase of the spread of COVID-19 as an autocatalytic process and have shown that the predicted dynamics of the viral transmission process match very well with the experimental data [32] (Section 7).

A molecular interpretation of the observed constancy of slope of the early spread is provided in terms of the autocatalytic framework, and the rate-limiting step of viral transmission has been identified. Finally, some constructive suggestions on therapeutic interventions for COVID-19 have been made.

## 2. Methods

Elementary unimolecular reversible or irreversible reactions and their series networks involving two or three chemical species are selected to illustrate our novel approach, and establish topological equivalence between the chemical and electrical representations. The electrical analog approach is subsequently extended to cover bimolecular, autocatalytic, and nonlinear reaction networks. The reaction networks are simulated by modeling each species as a capacitor ( $C_A$  and  $C_B$  in Fig. 1) with a capacity of 1 Farad. The initial voltage across the capacitor is set to represent the initial concentration of the corresponding species (100 V for a reactant and 0 V for all intermediates and products). Each reaction is modeled by allowing a resistor to drain a current from the reacting species capacitor to the ground. This resistor ( $R_{AB}$  in Fig. 1) has a value of resistance that is inversely proportional to the rate constant of the reaction. A zero volt dummy voltage source ( $V_{AB}$  in Fig. 1) is connected in series with this resistor to measure the current through this branch of the circuit. The current flowing through the resistor models the consumption of a particular reactant. To model the production of the product, the *same* current is made to flow into the product capacitor using a current-controlled current source ( $F_{AB}$ ; see Fig. 1). The dynamics of the system is studied by using the electrical simulation software SPICE [26] and plotting the variation of the voltage across the species capacitors as a function of time. The output plot of the concentration profile i.e., exponential decrease in A and exponential increase in B, exactly matches the results obtained by standard differential equation methods in chemical kinetics [1,2,5,7].

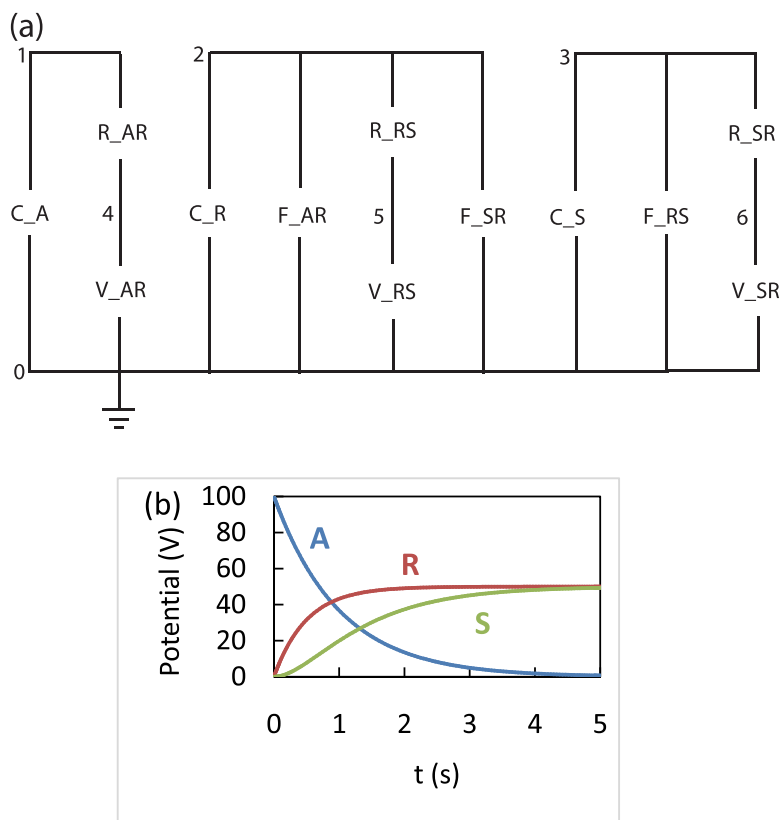


**Fig. 2.** (a) Electrical network analog for modeling the series reaction  $A \xrightarrow{1} R; R \xrightarrow{1} S$ . (b) Dynamics of the series reaction scheme on simulation of the topologically-equivalent electrical network.

Using methods based on Kirchhoff's laws, we first establish the topological equivalence between our electrical circuit representation and the standard chemical formulation by considering the simple irreversible reaction  $A \xrightarrow{k} B$  and the circuit shown in Fig. 1. For a first-order reaction, in the standard chemical model, we have

$$\frac{d[A]}{dt} = -k[A], \quad \frac{d[B]}{dt} = k[A] \quad (1)$$

where  $k$  is the rate constant of the reaction and  $[A]$  and  $[B]$  denote the concentrations of species A and B at any time  $t$ . Solving this for the case  $[A](t=0) = [A]_0$  and  $[B](t=0) = 0$  yields the well-known result,

$$[A] = [A]_0 \exp(-kt), \quad [B] = [A]_0 \{1 - \exp(-kt)\} \quad (2)$$

For the electrical circuit in Fig. 1, applying Kirchhoff's Loop Law leads to

$$\frac{q}{C_A} + R_{AB} \frac{dq}{dt} + V_{AB} = 0 \quad (3)$$

where  $q$  denotes the charge on the capacitor  $C_A$ . If there is no external input,  $V_{AB} = 0$  and we obtain

$$R_{AB} \frac{dq}{dt} = -\frac{q}{C_A} \Rightarrow C_A R_{AB} \frac{dV_A}{dt} = -V_A \quad (4)$$

where  $V_A$  is the voltage drop across  $C_A$ . If the capacitances are set to 1 Farad, we have

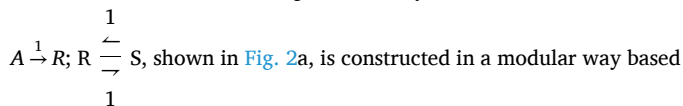
$$\frac{dV_A}{dt} = -\frac{V_A}{R_{AB}} \Rightarrow V_A = V_A(t=0) \exp\left(-\frac{t}{R_{AB}}\right) \quad (5)$$

which is identical to the form obtained when applying the law of mass action on the chemical reaction itself. Now, because of the current source in the second loop, we stipulate the currents in both loops to be identical. Hence the potential drop across capacitor  $C_B$  works out to be

$$V_B = \frac{q}{C_B} = V_A(t=0) \left\{ 1 - \exp\left(-\frac{t}{R_{AB}}\right) \right\} \quad (6)$$

The above results, given by Eqs. (5) and (6), are identical to those of the chemical version (Eq. (2)), and establish topological equivalence between the electrical and chemical formulations. Similar methods can be applied to different chemical reaction systems of increasing complexity.

The electrical circuit analog of a series system of chemical reactions,



The system is modeled by allowing the capacitor  $C_A$  to discharge through the resistor  $R_{AR}$  representing the chemical reaction  $A \rightarrow R$ . A zero volt voltage source is attached in the same branch as  $R_{AR}$  in order to measure the current flow through this resistor. This current flow is reproduced by the current-controlled current source (CCCS)  $F_{AR}$ , and is allowed to flow into  $C_R$ . For the reaction  $R \rightarrow S$ , a resistor  $R_{RS}$  is connected in parallel to  $C_R$ , and again a zero volt voltage source is connected to this resistor in series. Another CCCS,  $F_{RS}$  is used to reproduce this electrical current, and to feed it into  $C_S$ . Similarly, an equivalent set of elements is added for the reverse reaction  $S \rightarrow R$  (Fig. 2a).

The dynamics of the series system using our approach is illustrated in

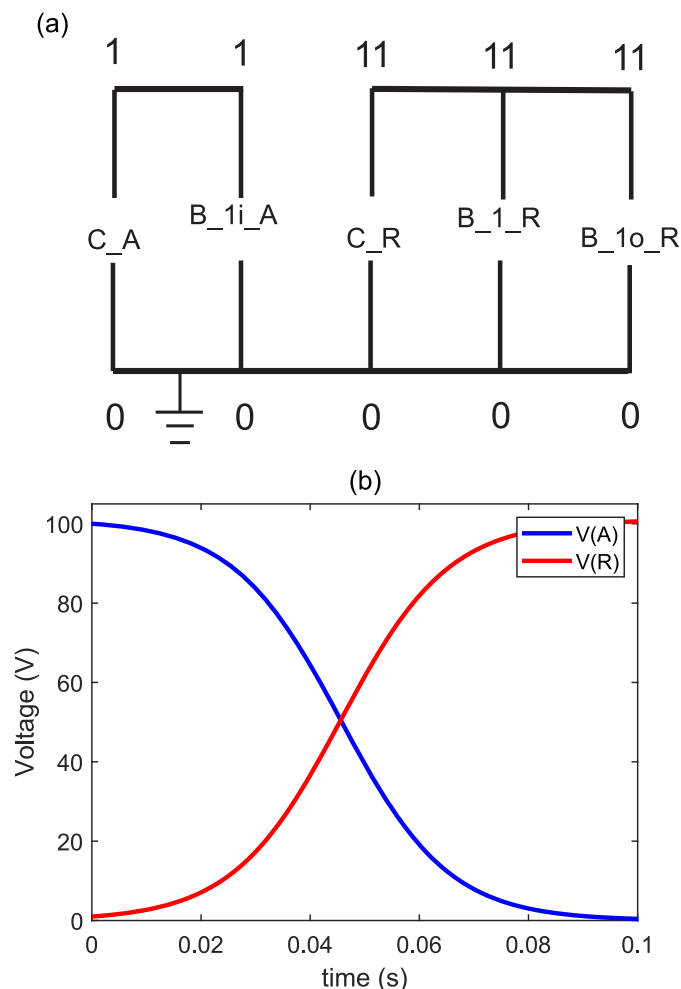


**Fig. 3.** (a) Equivalent electrical circuit for the second order irreversible autocatalytic reaction  $A + R \xrightarrow{1} 2R$  in shorthand notation.  $B$  represents a nonlinear current source. (b) Computer simulation of the dynamics of the irreversible autocatalytic reaction.

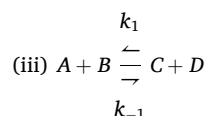
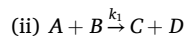
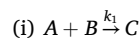
**Fig. 2b.** The results show that the concentration of  $A$  falls rapidly due to the irreversible  $A \rightarrow R$  reaction, but  $R$  and  $S$  reach a steady state with equal concentrations, their sum equaling the total  $A$  consumed until that point in time.  $S$  reaches the steady state concentration later than  $R$  because there is no route to directly convert  $A$  to  $S$ ; it has to come through  $R$ . Finally, note the initial time lag in the concentration profile for  $S$ , a characteristic of series reactions (Fig. 2b).

### 3. Dynamics of bimolecular and autocatalytic chemical reactions

Bimolecular and autocatalytic reactions and other *nonlinear* reaction networks are ubiquitous in chemical and biological systems. However they present unique problems while modeling them as equivalent electrical circuits that have not been resolved previously. The flux of the reaction in this case is dependent on more than one voltage, and this dependence is generally expressed as a product in chemical kinetics. The standard resistor which was used to model unimolecular reactions is no longer adequate for such bimolecular, autocatalytic, and nonlinear systems because the current flowing through the resistor can depend on only *one* voltage difference, that too in a linear way. The problem is solved here by using a new device, the nonlinear current source (NLCS). This device models a *nonlinear* resistor, and its current characteristics can be set to any mathematical function of the voltages and/or currents

in the electrical circuit. For the purpose of these simulations, the current characteristics are defined to be governed by the rate laws for the particular chemical reactions, written in terms of voltages instead of concentrations.

A set of three bimolecular elementary reactions were simulated to illustrate the above point. The selected sets were



Species in reactions (i) to (iii) were modeled as capacitors of capacity 1 Farad each, while the bimolecular chemical reaction was modeled by using sets of NLCSs as discussed above. For instance, in the case of reaction (iii) above, two NLCSs are used to remove an electric current equal to  $I(V) = k_1 V(A)V(B)$  from both capacitors  $A$  and  $B$ . Two more NLCSs are used to feed this same current into capacitors  $C$  and  $D$ . For the reverse reaction, which is also bimolecular, two NLCSs remove a current  $I(V) = k_{-1} V(C)V(D)$  from capacitors  $C$  and  $D$ , and two more are used to feed this current into capacitors  $A$  and  $B$ .

The equivalent electrical circuit for the second order irreversible autocatalytic reaction  $A + R \xrightarrow{1} 2R$  is shown in Fig. 3a, where the shorthand notation with  $B$  representing the nonlinear current source etc. is employed, which is convenient for use in large reaction networks. The NLCS,  $B_{1i\_A}$  withdraws a current from  $C\_A$  equal to the product of the concentration of  $A$  and  $R$ , and the rate constant. The same amount of current is also withdrawn by  $B_{1\_R}$  from  $C\_R$ . Twice the amount of this current is then fed into the capacitor  $C\_R$  by the NLCS,  $B_{1o\_R}$ . The dynamics of the irreversible autocatalytic reaction by the simulation is shown in Fig. 3b. The rate of formation of  $R$  increases with increase in the concentration of  $R$ , reaches a maxima when the product of the concentrations of  $A$  and  $R$  is a maximum, and then decreases to zero when nearly all  $A$  is converted to  $R$ .

The electrical analog for the second order reversible autocatalytic reaction  $A + R \xrightleftharpoons[1]{1} 2R$  is represented in Fig. 4a. The NLCS  $B_{1i\_A}$  with-

draws a current equal to the product of the concentration of  $A$  and  $R$ , and the rate constant from  $C\_A$ . The same current is also withdrawn by  $B_{1i\_R}$  from  $C\_R$ . Twice this current is then fed into the capacitor  $C\_R$  by the NLCS  $B_{1o\_R}$ . To model the reverse reaction,  $B_{2o\_R}$  withdraws from  $C\_R$  a current equal to the product of twice the square of the concentration of  $R$  and the rate constant. A current equal to the product of the square of the concentration of  $R$  and the rate constant is fed to  $C\_A$  and  $C\_R$  by  $B_{2i\_A}$  and  $B_{2i\_R}$ , respectively. Simulation of the analog reveals that the rate of formation of  $R$  increases with rise in the concentration of  $R$ . The rate of backward reaction is proportional to the square of the concentration of  $R$ . The concentration of  $R$  reaches a maximum value, although the rate of formation of  $R$  reaches zero (Fig. 4b).

### 4. Modeling the dynamics of autocatalytic reaction networks by circuit analog representations

Chemical reaction networks that contain autocatalytic reactions at their core are important in chemistry, biology and engineering. The Brusselator [9,22,23] is a classical nonlinear system that serves as a model for oscillating autocatalytic reactions whose dynamics are amenable to mathematical treatment by analytical methods and computer simulation. Such modeling of reaction dynamics also leads to an understanding of the onset of limit cycle oscillations which are very

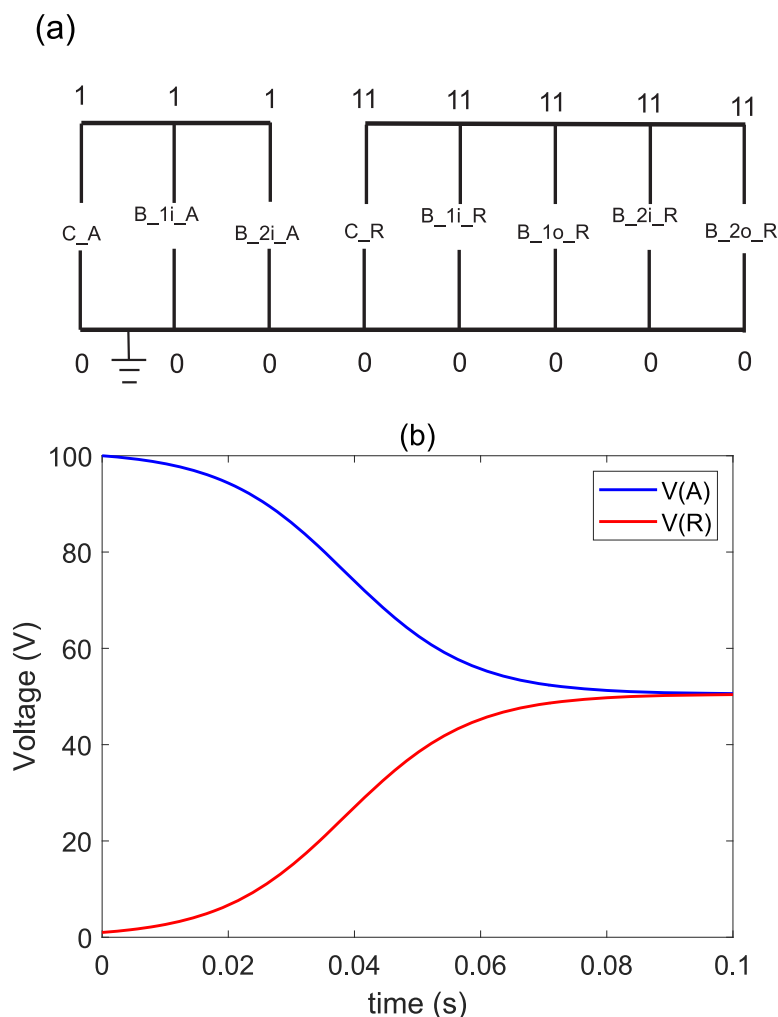


**Fig. 4.** (a) Electrical analog for the second order reversible autocatalytic reaction  $A + R \xrightleftharpoons[1]{1} 2R$ .  $B$  represents a nonlinear current source. (b) Computer simulation of the electrical analog in (a) using SPICE illustrates the dynamics of the reversible autocatalytic reaction.

important in nonlinear chemical and biological systems [2–10].

In the Brusselator autocatalytic model, one of the reacting species itself generates a catalytic intermediate that speeds up the production of the products. The model is described by the following set of chemical reactions:



The overall reaction is



Conventional analytical methods used to study such networks make a number of simplifying assumptions [22–25]. Our simulation approach using electrical analogs does not require these approximations. Another interesting aspect of modeling this nonlinear system as a circuit lies in the handling of non-unity stoichiometries in the autocatalytic reaction of

Eq. (8). Further, species  $X$  is a reactant as well as product in this reaction. The reaction is simulated by our novel approach using three NLCSS, two for withdrawing a current equal to  $I = k_2[V(X)]^2V(Y)$  from capacitor  $Y$ , and twice this current from capacitor  $X$ . The third NLCSS feeds thrice this current into capacitor  $X$  to simulate the production of three molecules of  $X$ . Other reactions are modeled as described in Section 3.

As discussed above, the different stoichiometric coefficients are incorporated into the circuit model through a gain factor introduced into the  $I(V)$  expression of the NLCSSs.  $A$  and  $B$  are in excess as per the postulates of the Brusselator model, and hence as such, the reaction cannot deplete them. These species are modeled in the equivalent circuit as standard voltage sources,  $V_A$  and  $V_B$ . The two intermediates in the reaction,  $X$  and  $Y$ , and the two products  $D$  and  $E$  are modeled as capacitors.

In brief, for reaction (7), a NLCSS  $B_{1X}$  feeds a current equal to the product of the concentration of  $A$  and the rate constant  $k_1$  into the capacitor  $C_X$ . No corresponding NLCSS is required for withdrawing this current from  $V_A$ , as the postulate in the model of excess  $A$  makes it unnecessary.

For reaction (8), the NLCSS  $B_{2iX}$  removes a current equal to twice the product of the square of the concentration of  $X$  and the concentration of  $Y$  with the rate constant of the reaction ( $k_2$ ) from the capacitor  $C_X$ . The NLCSS  $B_{2oY}$  removes this same current, but without the gain factor

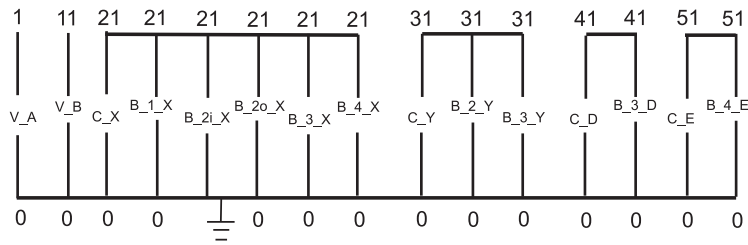


Fig. 5. Electrical analog of the nonlinear autocatalytic chemical reaction network of the Brusselator system described by Eqs. (7)–(10).

Table 1

Dynamical regimes of the Brusselator for different parameters of the system (see Sections 5 and 6).

Concentration of A	Concentration of B	Classification of nonlinear dynamics
2	0.5	Stable node
1	1.8	Stable focus
1	2.0	Center
1	2.2	Unstable focus
1	5.0	Unstable node

of two from C.Y. Then, for the R.H.S. of the reaction, the NLCS B<sub>2o</sub>X feeds this same current, but with a factor of three, to C<sub>X</sub>. The circuit analog is depicted in Fig. 5. The NLCSs B<sub>2i</sub>X and B<sub>2o</sub>X can be combined together with a net B<sub>2</sub>X with an I(V) equal to the sum of the I(V)s of B<sub>2i</sub>X and B<sub>2o</sub>X. However, for clarity and consistency and the modular nature of our approach, these elements are kept separate in the representation of Fig. 5.

For reaction (9), the NLCS B<sub>3</sub>X removes current equal to the product of the concentrations of B and X with the rate constant from C<sub>X</sub>. No corresponding NLCS is added in the circuit representation shown in Fig. 5 for withdrawing this amount of current from V<sub>B</sub> given that V<sub>B</sub> is a voltage source. The same current is fed by the NLCSs B<sub>3</sub>D and B<sub>3</sub>Y into capacitors C<sub>D</sub> and C<sub>Y</sub>.

For reaction (10), the NLCS B<sub>4</sub>X removes a current equal to the product of the concentration of X with the corresponding rate constant from C<sub>X</sub> and feeds it into C<sub>E</sub> (see Fig. 5).

The values of all the rate constants appearing in the system of reactions given by Eqs. (7)–(10) are fixed as unity, following common practice and for convenience [22,23]. These values can be readily changed in the circuit analog of Fig. 5, and the analog can be re-simulated for altered values of the kinetic parameters. However, before the circuit analog shown in Fig. 5 can be simulated, and the rich and diverse behavioural patterns and instabilities of the nonlinear system identified, we need to determine the various sets of the concentrations of A and B for which characteristic patterns and configurations emerge. This requires a mathematical analysis of the local stability of the system as a function of the parameters of the nonlinear system. Such an analysis is carried out in Section 5. Following this analysis, the dynamics of the system can be readily simulated for representative classes (Section 6).

## 5. Stability analysis of the reaction network

Considering the mass action law for the reaction intermediates of the Brusselator leads to the following rate equations:

$$\frac{dX}{dt} = F(X, Y) = A + X^2Y - BX - X \quad (12)$$

$$\frac{dY}{dt} = G(X, Y) = BX - X^2Y \quad (13)$$

The concentrations of species A and B are kept constant in space and time in the reactor. At the stationary steady state, the concentrations of species X and Y are space and time independent, and the derivatives on

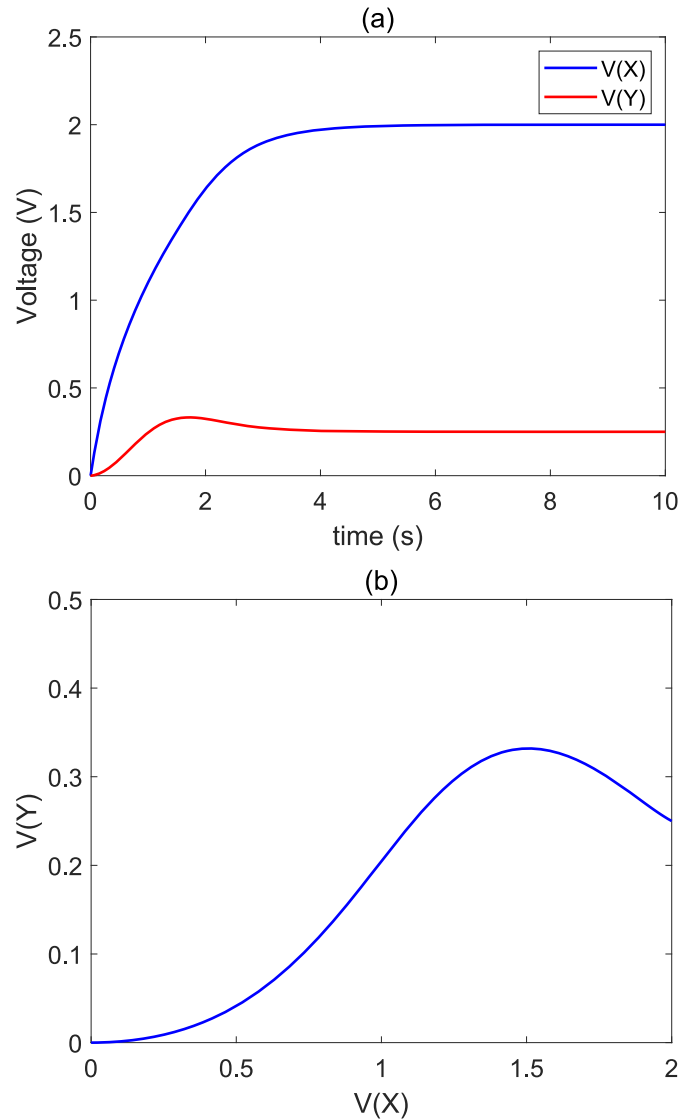


Fig. 6. Simulation of the electrical analog of the Brusselator shown in Fig. 5: Dynamics of the system for  $A = 2.0$ ,  $B = 0.5$ . The system monotonically relaxes to the fixed point without oscillations upon perturbation (stable node). (a) Decay of the concentrations of X and Y with time. (b) Phase plane plot of X and Y.

the L.H.S. of Eqs. (12) and (13) vanish. This leads to the stationary steady state solution

$$X_{ss} = A \quad (14)$$

$$Y_{ss} = \frac{B}{A} \quad (15)$$



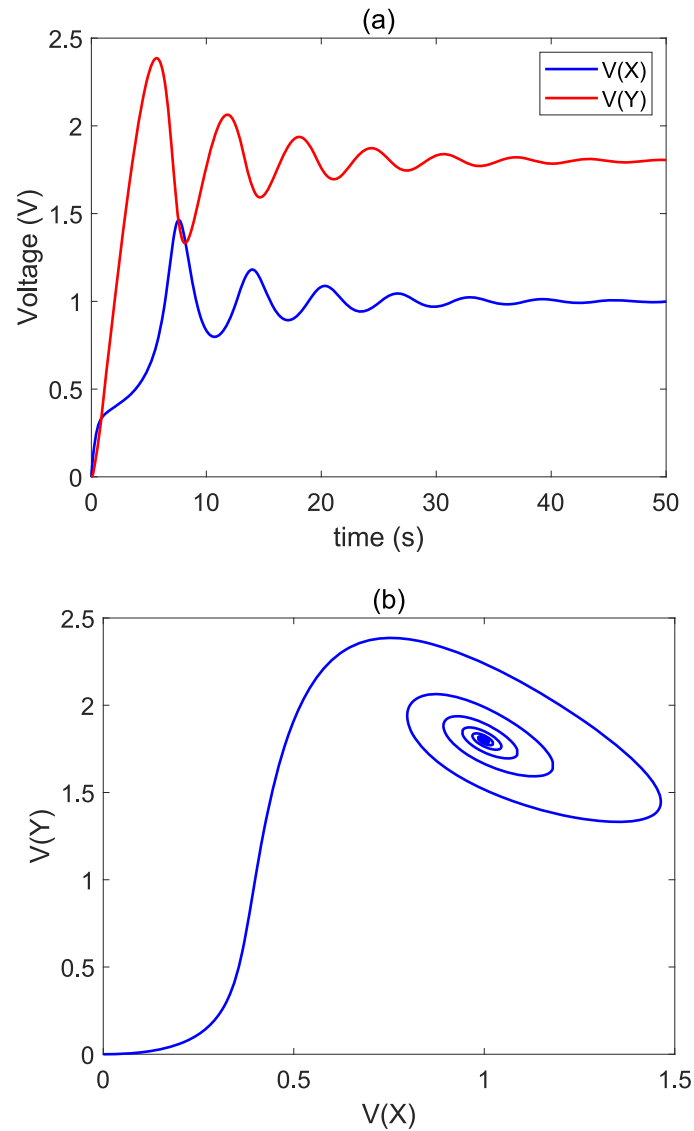


**Fig. 7.** Dynamics of the Brusselator system for  $A = 1.0$ ,  $B = 1.8$  obtained by simulation of the electrical analog shown in Fig. 5. For these parameters the system exhibits damped oscillations (stable focus). (a) Plot of  $X$ ,  $Y$  versus time. (b) Phase plane plot of  $XY$ .

The linear stability of the Brusselator can be determined via the Jacobian [9] of the system of Eqs. (12) and (13), i.e.

$$\mathbf{J} = \begin{bmatrix} \frac{\partial F}{\partial X} & \frac{\partial F}{\partial Y} \\ \frac{\partial G}{\partial X} & \frac{\partial G}{\partial Y} \end{bmatrix} = \begin{bmatrix} 2XY - (1+B) & X^2 \\ B - 2XY & -X^2 \end{bmatrix} \quad (16)$$

Evaluating the Jacobian at the fixed point of the stationary steady state given by Eqs. (14) and (15) leads to

$$\mathbf{J}_{ss} = \begin{bmatrix} B-1 & A^2 \\ -B & -A^2 \end{bmatrix} \quad (17)$$

We can evaluate the linear stability of the stationary steady state by solving the eigenvalue equation of the Jacobian

$$\det \begin{bmatrix} B-1-\lambda & A^2 \\ -B & -A^2-\lambda \end{bmatrix} = 0 \quad (18)$$

where  $\lambda$  stands for the eigenvalues. This yields the characteristic equation

$$\lambda^2 + (1+A^2-B)\lambda + A^2 = 0 \quad (19)$$

The two eigenvalues are given by

$$\lambda_{1,2} = \frac{1}{2}(B-1-A^2) \pm \frac{1}{2}\sqrt{(B-1-A^2)^2 - 4A^2} \quad (20)$$

The discriminant,  $\Delta$  is expressed as

$$\Delta = [(B-1-A^2)^2 - 4A^2] \quad (21)$$

The linear stability and dynamical behavior can be evaluated by determining the values/signs of the trace and discriminant of the Jacobian matrix at the stationary steady state or fixed point of the system [9]. These are given by the equations

$$\text{trace}(\mathbf{J}_{ss}) = B-1-A^2 \quad (22)$$

$$\det(\mathbf{J}_{ss}) = A^2 > 0 \quad (23)$$

For  $\Delta > 0$ , the system eigenvalues are real. If  $\text{trace}(\mathbf{J}_{ss}) < 0$ , i.e. for  $B < (1+A^2)$ , the eigenvalues  $\lambda_1, \lambda_2$  are negative and real, and the steady state is a stable node. Thus a small perturbation of the steady state monotonically decreases and the system rapidly relaxes back to the steady state. If  $\text{trace}(\mathbf{J}_{ss}) > 0$ , i.e. for  $B > (1+A^2)$ , the eigenvalues  $\lambda_1, \lambda_2$  are positive and real, and the steady state is an unstable node, i.e. a small

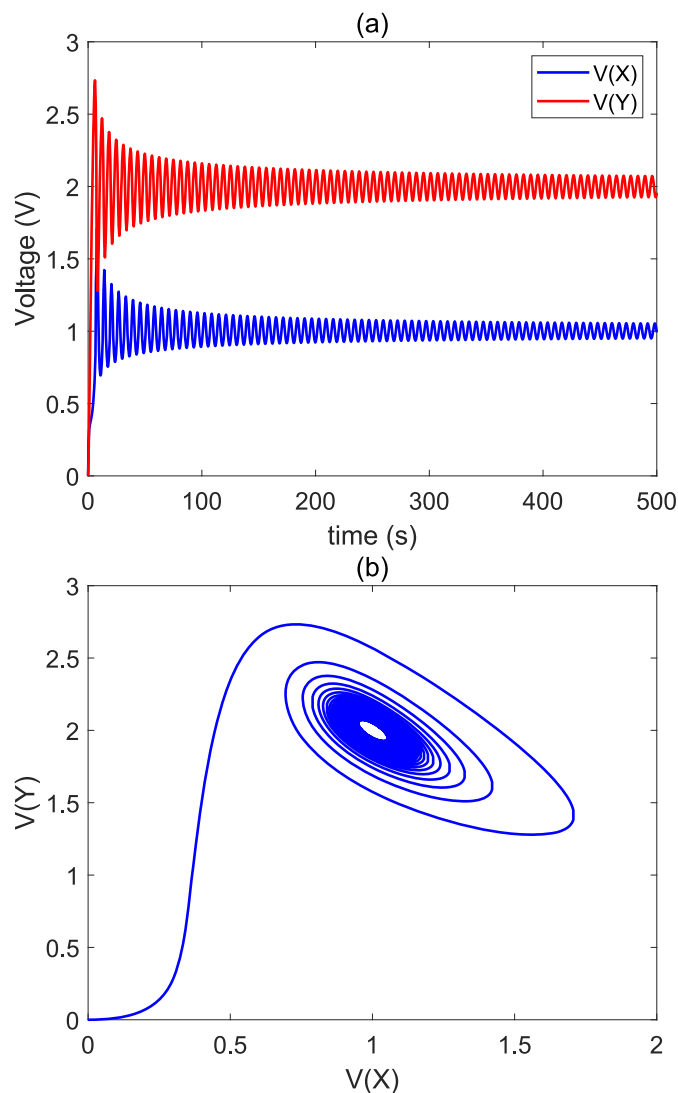


**Fig. 8.** Dynamics of the Brusselator system for  $A = 1.0$ ,  $B = 2.0$  obtained by simulation of the electrical analog shown in Fig. 5. Limit cycle behavior is observed for these parameters. (a) Plot of  $X$ ,  $Y$  versus time showing a center. (b) Phase plane plot in  $XY$  coordinates.

perturbation dynamically moves the system away from the steady state.

For  $\Delta < 0$ , the eigenvalues are complex conjugate pairs, and the system is oscillatory. If  $\text{trace}(J_{ss}) < 0$ , i.e. for  $B < (1 + A^2)$ , upon a small perturbation, the steady state will oscillate and relax back to the steady state (stable focus). If  $\text{trace}(J_{ss}) > 0$ , i.e. for  $B > (1 + A^2)$ , the amplitude of the oscillations increases with time and the system is characterized as an unstable focus. If  $\text{trace}(J_{ss}) = 0$ , i.e.  $B = (1 + A^2)$ , and the roots are purely imaginary, and the system shows a cyclic movement around the steady state (center), and a limit cycle with periodic oscillation is observed.

The five prototypical stability/instability regions for the Brusselator based on the above analytical linear stability analysis are tabulated in Table 1.

## 6. Simulation of system dynamics of the Brusselator

The electrical network analog represented by Fig. 5 is now simulated for various sets of concentrations of  $A$  and  $B$ . The circuit displays several interesting behavioral patterns that can be classified into various categories (Table 1). The concentration of the intermediates  $X$  and  $Y$  are plotted with time, along with phase plane  $XY$  plots (Figs. 6–10) to better

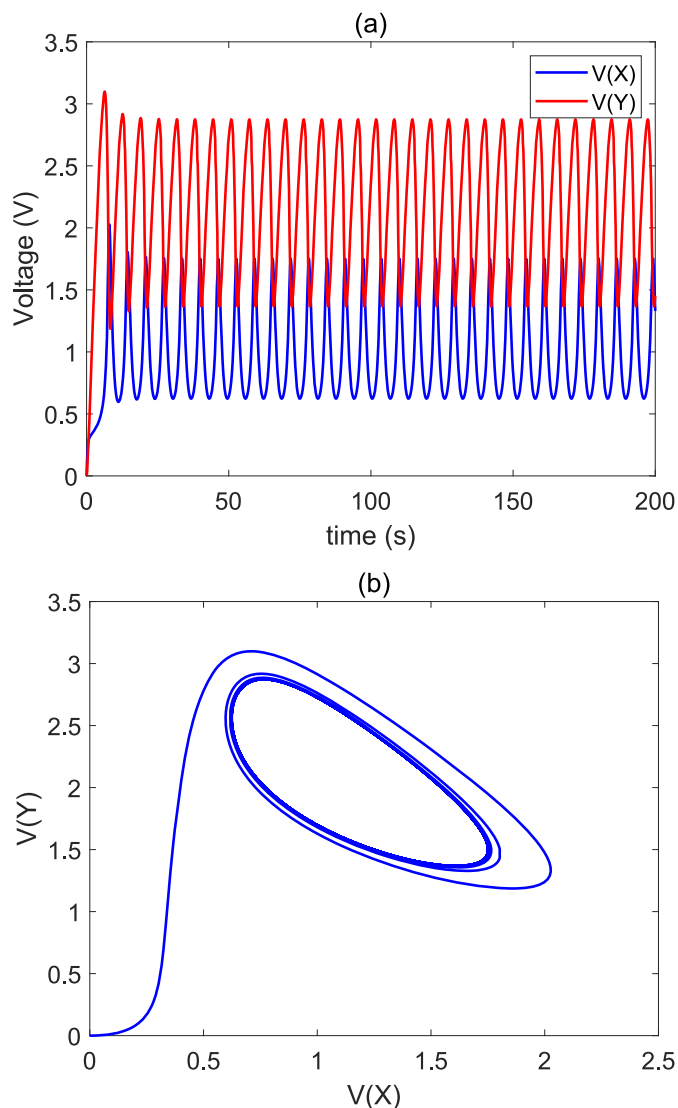


**Fig. 9.** Dynamics of the Brusselator system for  $A = 1.0$ ,  $B = 2.2$  obtained by simulation of the electrical analog. The system exhibits an unstable focus. (a) Plot of  $X$ ,  $Y$  versus time. (b) Phase plane plot in  $XY$  coordinates.

illustrate the system dynamics. Because of the graphical nature of the electrical network approach, it is easy to change the topology of the model and study the effect of the change on the system dynamics.

Figs. 6–10 represent plots of the evolution of the concentrations of the reaction intermediates of the Brusselator generated by simulation of the electrical circuit shown in Fig. 5 for variation of the parameters of the system. The set of parameters selected are representative of the various dynamical patterns given in Table 1.

For  $A = 2.0$  and  $B = 0.5$ , the perturbed system decays rapidly to the stationary steady state  $(X_{ss}, Y_{ss}) = (A, B/A) = (2, 0.25)$  without oscillation. This is clearly seen from the simulation plot of  $X$  and  $Y$  as a function of time and also from the  $XY$  phase plane plot (Fig. 6a and 6b), and is readily classified as a stable node.

For  $A = 1.0$  and  $B = 1.8$ , the system exhibits damped oscillation, and can be classified as a stable focus (Fig. 7). The nature of the oscillating system changes qualitatively at the Hopf bifurcation point  $A = 1.0$  and  $B = 2.0$ , and an orbiting pattern about the fixed point and a limit cycle of undamped oscillation emerges (Fig. 8), in accordance with the Poincaré classification of Table 1. This happens principally because the eigenvalues in Eq. (20) are purely imaginary, since  $B = (1 + A^2)$ . The frequency of the oscillation is given analytically by  $\frac{\sqrt{\det J_{ss}}}{2\pi} = 1/2\pi$  for this



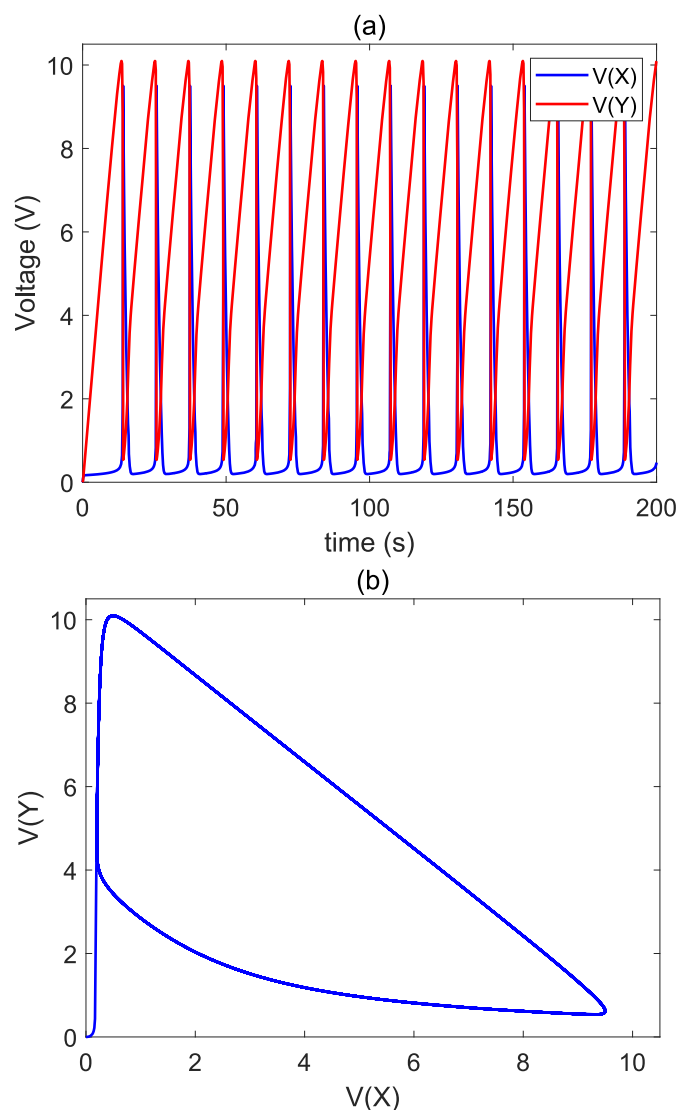


Fig. 10. Dynamics of the Brusselator system for  $A = 1.0$ ,  $B = 5.0$  obtained by simulation of the electrical analog showing unstable node-type nonlinear behavior. (a) Plot of  $X$ ,  $Y$  versus time. (b) Phase plane plot in  $XY$  coordinates.

particular case, as verified by simulation of the electrical circuit analog (Fig. 8a). For  $A = 1.0$  and  $B = 2.2$ , the amplitude of the oscillation increases (unstable focus) as seen by comparison of Fig. 9a with Figs. 7a and 8a.

Finally, as  $B$  increases beyond a limit (for constant  $A$ ), there is virtually no oscillation within the time scale of the simulation, and the behavior can be classified as a type of unstable node (Fig. 10).

## 7. Application to biological systems: the early onset of spread of COVID-19 modeled as an autocatalytic process

The above discussion should not be taken to imply that the methods developed are applicable only to chemical reactions; in fact, the methods are quite general. Taking the modeling of the COVID-19 pandemic as an example, it is shown in this Section that the approach can be applied to other autocatalytic processes, and that such modeling leads to novel mechanistic insights into the mode of viral transmission.

Current epidemiological approaches to modeling the spread of the pandemic are generally based on the classical SIR scheme [27]. This scheme divides the population into Susceptible ( $S$ ), Infectious ( $I$ ), and Removed ( $R$ ) pools within the population, and assumes that the

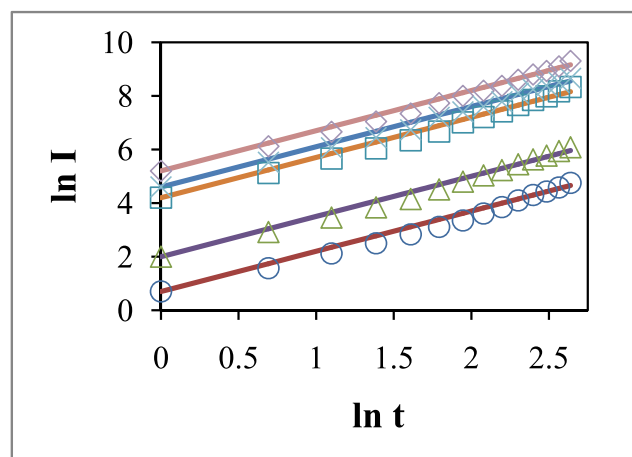


Fig. 11. Log-log plot of fourteen-day early phase of spread of the COVID-19 pandemic in Europe after reaching one confirmed case per million during the first half of 2020. X-axis: time in days; Y-axis: Total cases per million per sq. km. Symbols represent data [31], and lines represent simulation of an autocatalytic model of viral transmission (see Section 7). The slope of the straight lines in the Figure is given by  $1/(1 - n)$ , with  $n = 0.33$ . See the text for a molecular interpretation of the observed constancy of the slope of the straight lines.

transmission follows a first-order rate law with respect to the infectious agent/sub-population/intermediate, which leads to exponential growth. However, by analyzing actual data on the early onset of the spread of COVID-19 in several countries, it is shown here that the growth of cases does not follow exponential kinetics. Rather it obeys a *power law* for the concentration of the infectious intermediate,  $[I]$  as a function of time. Such behavior of  $I$  is realistically modeled by considering the transmission as an *autocatalytic process of order  $n$* . Simulation of the transmission process reveals the finding that  $n$  is identically equal to 0.33, as extracted from the slope of the straight lines in Fig. 11. This regularity is shown to offer a wealth of molecular and mechanistic insights into the rate-limiting step of viral transmission and spread of the pandemic.

With the above insights, the kinetics of spread of the pandemic can be represented by the general kinetic scheme



The general rate equation can be written as

$$\frac{dI}{dt} = k' I^n - k_r I \quad (26)$$

where  $k'$  and  $k_r$  are the rate constants of the elementary steps given by Eqs. (24) and (25) respectively. The SIR scheme of classical epidemiology [27] can be viewed as a special case of Eq. (26) with  $n = 1$ .

In the early phase of the pandemic,  $k_r I$  is small, and further, the population density of susceptible individuals can be taken as a constant. Hence, we need to track only the number density of the total infections (confirmed cases) in a population, and

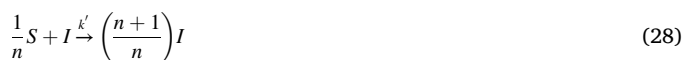
$$\frac{dI}{dt} = k' I^n \quad (27)$$

Data on the spread of the pandemic during its early stage for several countries in Europe [31] was taken from the Johns Hopkins database accessed via Github [32]. Early stage is interpreted here as the number of cases during a 14-day time-period after detection of the first confirmed case. In Fig. 11, the normalized number density of confirmed cases versus time is shown by the data points, and the best-fit from the simulation is shown by the bold lines. The slope of the straight lines in Fig. 11 is given by  $1/(1 - n)$ , with  $n = 0.33$ .

Further analysis of the data for Europe, Asia, and America reveals that, although the apparent rate constant  $k$  in Eq. (27) varies from region to region, the value of  $n$  is a constant that is a characteristic of the transmission process, with  $n = 0.33 \pm 0.05$ . This constancy of  $n$  (Fig. 11) and its lack of dependence on environmental factors imply that  $n$  is a determinant of the reaction mechanism and an *intrinsic* property of the infection process. This suggests a possible molecular mechanistic explanation with regard to the structure and function of SARS-CoV-2.

The finding of a constant  $n = 0.33$  that is a characteristic of viral transmission (Fig. 11) suggests that the SARS-CoV-2 spike protein is a *trimer* (since  $1/n = 3$ ), which is experimentally supported by cryo-EM structural data [33–35]. Further, the implication suggests itself that interaction and binding of the trimer on the virion in its inactive pre-fusion state via its three receptor binding domains [35] with clustered host cell receptors lead to the formation of an activated postfusion state of the complex that mediates the autocatalytic process of cell entry of the virus. This is the essential, rate-limiting step that promotes cell entry of SARS-CoV-2 and leads to further downstream steps of viral replication and infection.

Given the above interpretation, a molecular scheme for autocatalytic viral transmission with  $1/n = 3$  in Eqs. (24), (25) can be written as



A consequence of the above is that medical interventions that repress infection after viral cell entry as per Eq. (29) would only be of marginal utility in controlling disease transmission. Effective intervention strategies therefore need to block the rate-limiting step of formation of the postfusion state after cell-receptor interactions that mediate entry of the SARS-CoV-2 virus into the human cell (Eq. (28)).

## 8. Conclusions

A general, novel methodology for representation, visualization, and quantification of the dynamics of nonlinear chemical reaction networks using electrical analogs has been developed. Topological equivalence of the electrical analog has been mathematically proved using Kirchhoff's laws for unimolecular reactions. The modular approach has been extended to complex biomolecular, autocatalytic reactions, and their nonlinear networks by using nonlinear electrical elements. The nonlinear dynamical patterns and configurations of the various regimes in the reaction network of the Brusselator have been elucidated by stability analysis and validated by computer simulation of the nonlinear electrical analog. It has been shown that the developed methods can be applied to other processes. A realistic example has been taken of the early phase of spread of the COVID-19 pandemic modeled as an autocatalytic process – as opposed to first-order kinetics assumed by the standard model. Excellent agreement of prediction with experiment has been obtained, and new molecular insights into the process of viral transmission have been offered. In summary, the developed model using electrical analogs is novel, elegant, employs a modular approach, enables fast simulation, and accommodates easy modification of network elements, structure, and connectivity for elucidating reaction dynamics.

## Funding information

No funding was received for this work.

## Declaration of Competing Interest

The authors declare that they have no known competing financial interests or personal relationships that could have appeared to influence the work reported in this paper.

## References

- [1] H.S. Fogler, Elements of Chemical Reaction Engineering, 6th ed., Pearson, London, 2021.
- [2] J. Villadsen, J. Nielsen, G. Lidén, Bioreaction Engineering Principles, 3rd ed., Springer, New York, 2011.
- [3] C. Kuntz, C. Kuhn, H. Weickenmeier, et al., Kinetic modelling and simulation of high-temperature by-product formation from urea decomposition, Chem. Eng. Sci. 246 (2021), 116876.
- [4] P. Li, X. Zeng, Z. Li, Understanding high-temperature chemical reactions on metal surfaces, J. Am. Chem. Soc. Au 2 (2022) 443–452.
- [5] M.T. Klann, A. Lapin, M. Reuss, Agent-based simulations of reactions in the crowded and structured intracellular environment, BMC Syst. Biol. 5 (2011) 71.
- [6] M.S. Kwon, B.T. Lee, S.Y. Lee, H.U. Kim, Modeling regulatory networks using machine learning for systems metabolic engineering, Curr. Opin. Biotechnol. 65 (2020) 163–170.
- [7] J. Villadsen, Fundamental Bioengineering, Wiley-VCH, Weinheim, 2016.
- [8] W. Dong, M.A. Keibler, G. Stephanopoulos, Review of metabolic pathways activated in cancer cells as determined through isotopic labeling and network analysis, Metab. Eng. 43 (2017) 117–124.
- [9] I.R. Epstein, J. Pojman, An Introduction to Nonlinear Chemical Dynamics: Oscillations, Waves, Patterns, and Chaos, Oxford University Press, New York, 1998.
- [10] L.O. Chua, C.A. Desoer, E.S. Kuh, Linear and Nonlinear Circuits, McGraw-Hill, New York, 1987.
- [11] W.L. Luyben, Process Modeling, Simulation, and Control for Chemical Engineers, 2nd ed., McGraw-Hill, New York, 1996.
- [12] C. Witkov, Bond graphs: graphical cross-disciplinary systems modeling based on power and energy relations, GRC Physics Research and Education, Novel Research in Energy Topics, Smithfield, RI, USA, 2018.
- [13] Y. Chen, Z. Wang, Y.W. Harn, et al., Resolving optical and catalytic activities in thermoresponsive nanoparticles by permanent ligation with temperature-sensitive polymers, Angew. Chem. Int. Ed. 58 (2019) 11910–11917.
- [14] D. Yang, Y. Chen, H. Peng, et al., An integrated experimental and theoretical study on the optical properties of uniform hairy noble metal nanoparticles, Nanoscale 10 (2018) 22750.
- [15] P. Gray, S. Scott, Autocatalytic reactions in the isothermal continuous stirred tank reactor: oscillations and instabilities in the system  $A + 2B \rightarrow 3B$ ;  $B \rightarrow C$ , Chem. Eng. Sci. 39 (1984) 1087–1097.
- [16] J. Kumar, S. Nath, Analysis of autocatalytic reactions with Michaelis-Menten kinetics in an isothermal continuous stirred tank reactor, Chem. Eng. Sci. 52 (1997) 3455–3462.
- [17] T.R. Marchant, Cubic autocatalysis with Michaelis-Menten kinetics: semi-analytical solutions for the reaction-diffusion cell, Chem. Eng. Sci. 59 (2004) 3433–3440.
- [18] A. Khot, S. Pushpavanam, Coupled autocatalytic reactions: interconversion and extinction of species, Chem. Eng. Sci. 160 (2017) 254–268.
- [19] W.S. Lin, E. Kussell, L.S. Young, C. Jacobs-Wagner, Origin of exponential growth in nonlinear reaction networks, Proc. Natl. Acad. Sci. USA. 117 (2020) 27795–27804.
- [20] W. Wiechert, Modeling and simulation: tools for metabolic engineering, J. Biotechnol. 94 (2002) 37–63.
- [21] M. Ederer, E.D. Gilles, Thermodynamically feasible kinetic models of reaction networks, Biophys. J. 92 (2007) 1846–1857.
- [22] P. Glansdorff, I. Prigogine, Thermodynamic Theory of Structure, Stability and Fluctuations, Wiley, New York, 1971.
- [23] J.J. Tyson, Some further studies of nonlinear oscillations in chemical systems, J. Chem. Phys. 58 (1973) 3919–3930.
- [24] E.E. Selkov, Self-oscillations in glycolysis. A simple kinetic model, Eur. J. Biochem. 4 (1968) 79–86.
- [25] A. Pellissier-Tanon, G. Morgado, L. Jullien, A. Lemarchand, Quasi-steady-state and partial-equilibrium approximations in chemical kinetics: one stage beyond the elimination of a fast variable, ChemRxiv (2021), 10.26434/chemrxiv.14198768.v2.
- [26] G.W. Roberts, A.S. Sedra, SPICE, 2nd ed., Oxford University Press, New Delhi, 2010.
- [27] W.O. Kermack, A.G. McKendrick, A contribution to the mathematical theory of epidemics, Proc. R. Soc. A 115 (1927) 700–721.
- [28] A.L. Bertozzi, E. Franco, G. Mohler, M.B. Short, D. Sledge, The challenges of modeling and forecasting the spread of COVID-19, Proc. Natl. Acad. Sci. USA. 117 (2020) 16732–16738.
- [29] F. Manenti, A. Galeazzi, F. Bisotti, K. Prifti, A. Dell'Angelo, A. Di Pretoro, C. Ariatti, Analogies between SARS-Cov-2 infection dynamics and batch chemical reactor behaviour, Chem. Eng. Sci. 227 (2020), 115918.
- [30] N.L. Komarova, L.M. Schang, D. Wodarz, Patterns of the COVID-19 pandemic spread around the world: exponential versus power laws, J. R. Soc. Interface 17 (2020), 20200518.
- [31] S. Nikita, R. Anand, A.S. Rathore, A chemical engineer's take of COVID-19 epidemiology, AIChE J. 67 (2021) e17359.
- [32] <https://github.com/owid/covid-19-data/tree/master/public/data>, 2021.
- [33] D. Wrapp, N. Wang, K.S. Corbett, et al., Cryo-EM structure of the 2019-nCoV spike in the prefusion conformation, Science 367 (2020) 1260–1263.
- [34] C. Xu, Y. Wang, C. Liu, et al., Conformational dynamics of SARS-CoV-2 trimeric spike glycoprotein in complex with receptor ACE2 revealed by cryo-EM, Sci. Adv. 7 (2021) eabe5575.
- [35] L. Guo, W. Bi, X. Wang, et al., Engineered trimeric ACE2 binds viral spike protein and locks it in “Three-up” conformation to potentially inhibit SARS-CoV-2 infection, Cell Res. 31 (2021) 98–100.